IOP Publishing Measurement Science and Technology
Meas. Sci. Technol. **26** (2015) 055103 (12pp) doi:10.1088/0957-0233/26/5/055103

Network of flexible capacitive strain gauges for the reconstruction of surface strain

Jingzhe Wu[1], Chunhui Song[1], Hussam S Saleem[1], Austin Downey[1] and Simon Laflamme[1,2]

[1] Department of Civil, Construction, and Environmental Engineering, Iowa State University, Ames, IA 50011, USA
[2] Department of Electrical and Computer Engineering, Iowa State University, Ames, IA 50011, USA

E-mail: jingzhe@umd.edu.

Received 2 October 2014, revised 24 February 2015
Accepted for publication 5 March 2015
Published 9 April 2015

Abstract

Monitoring of surface strain on mesosurfaces is a difficult task, often impeded by the lack of scalability of conventional sensing systems. A solution is to deploy large networks of flexible strain gauges, a type of large area electronics. The authors have recently proposed a soft elastomeric capacitor (SEC) as an economical skin-type solution for large-scale deployment onto mesosurfaces. The sensing principle is based on a measurable change in the sensor's capacitance upon strain. In this paper, we study the performance of the sensor at reconstructing surface strain map and deflection shapes. A particular feature of the sensor is that it measures surface strain additively, because it is not utilized within a Wheatstone bridge configuration. An algorithm is proposed to decompose the additive in-plane strain measurements from the SEC into principal components. The algorithm consists of assuming a polynomial shape function, and deriving the strain based on Kirchhoff plate theory. A least-squares estimator (LSE) is used to minimize the error between the assumed model and the SEC signals after the enforcement of boundary conditions. Numerical simulations are conducted on a symmetric rectangular cantilever thin plate under symmetric and asymmetric static loads to demonstrate the accuracy and real-time applicability of the algorithm. The performance of the algorithm is further examined on an asymmetric cantilever laminated thin plate constituted with orthotropic materials mimicking a wind turbine blade, and subjected to a non-stationary wind load. Results from simulations show good performance of the algorithm at reconstructing the surface strain maps for both in-plane principal strain components, and that it can be applied in real time. However, its performance can be improved by strengthening assumptions on boundary conditions. The algorithm exhibits robustness in performance with respect to load and noise in signals, except when most of the sensors' signals are close to zero due to over-fitting form the LSE.

Keywords: surface strain, deflection shape, shape reconstruction, soft elastomeric capacitor, structural health monitoring, large area electronics, skin sensor

(Some figures may appear in colour only in the online journal)

1. Introduction

Condition assessment of geometrically large systems, termed mesosystems, which include transportation infrastructures, aerospace structures, and energy systems, is a difficult task due to the large surfaces that require monitoring. The majority of existing sensing solutions have technical and/or economic obstacles that limit their scalability, thus impeding their applicability [1, 2]. Because it is clear, in some applications, that condition assessment has strong potential benefits, there is a growing interest in developing sensing solutions that are deployable at large scales. In particular, it has been thoroughly

 © 2015 IOP Publishing Ltd Printed in the UK

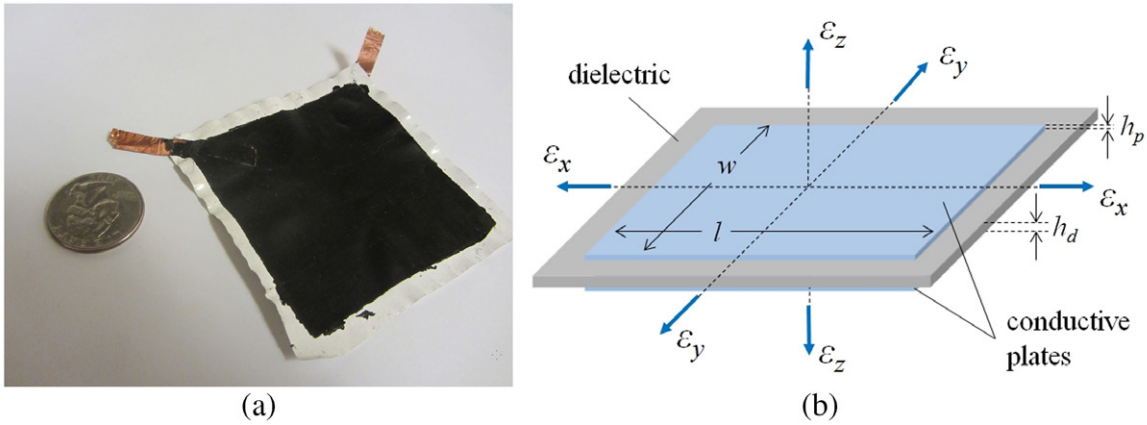

Figure 1. (*a*) A single SEC ($70 \times 70\,\mathrm{mm}^2$); and (*b*) schematic representation of the SEC.

discussed that monitoring of wind turbine blades may lead to important reductions in the cost of wind turbine operation and maintenance, which would decrease costs associated with wind energy production [3–5].

To enable the monitoring of mesosystems, the authors have recently proposed a large flexible soft elastomeric capacitor (SEC) [2, 6]. The sensing principle is based on a measurable change in the sensor's capacitance upon strain. Analogous to biological skin, several SECs can be arranged in a network configuration to measure discrete surface strain over large surfaces, as demonstrated in [7] for uni-axial strain. Other skin-type sensors have been proposed including large sensing sheets of strain gauges [8, 9], resistance-based thin-films fabricated by leveraging the high conductivity of carbon nanotubes [10–13] and capacitance-based sensors for strain [14], pressure [15], triaxial force [16], and humidity [17, 18] measurements. The SEC investigated herein differs from the literature by combining high scalability, low-cost fabrication, and mechanical robustness.

The utilization of such dense sensor networks enables the collection of vast arrays of strain data on mesosurfaces. It is thus possible to conduct condition assessment by reconstructing surface features, such as strain maps and deflection shapes, and examining temporal changes within features that can be correlated to altered structural conditions. The reconstruction of strain maps from displacement data has been proposed using digital image correlation from displacement field data [19, 20]. Algorithms have also been proposed to reconstruct deflection shapes from strain data based on the inverse finite element method [21–23], and by directly integrating strain data [24–26]. Others have studied the reconstruction of strain maps directly from strain data using shape functions either derived from plate theory [27–29] or approximated [30, 31].

The algorithms presented in the literature for strain map and deflection shape reconstruction from strain data require knowledge of the strain magnitude and direction. Unlike most strain sensing methods, the SEC developed by the authors measures the additive in-plane strain components. It follows that both the principal strain magnitudes and directions are hidden in the information. To fully enable the applications of SECs for condition assessment of mesosurfaces, an algorithm must be developed to retrieve the hidden information used in feature reconstruction.

Here, we propose to leverage the network configuration in the SEC application to decompose the additive strain measurements and reconstruct strain maps and deflection shapes. The objective is to enable real-time acquisition of these condition assessment features from SEC data. The algorithm consists of assuming a shape deformation consistent with boundary conditions, and deriving 2D strain functions. A least-squares estimator (LSE) is used to obtain the best-fit result for the strain functions based on the measured additive strain values from the SEC. However, the formulation of the LSE from the additive sensor's signal creates multicollinearity. It results that the proposed algorithm relies on the quality of the assumptions made about the strain boundary conditions. The performance of the algorithm is verified on a symmetric thin plate subjected to symmetric and asymmetric static loads. Also, potential application on wind turbine blades is demonstrated by simulating an asymmetric cantilever laminated thin plate with orthotropic material resembling a wind turbine blade.

The paper is organized as follows. Section 2 derives the sensing principle and explains the additive strain sensing feature. Section 3 presents the strain decomposition algorithm, and validates the algorithm on a small scale laboratory experiment. Section 4 verifies the algorithm on a simple cantilever structure subjected to symmetric and asymmetric loads. Section 5 extends the simulations to an asymmetric laminated plate with orthotropic material properties mimicking a wind turbine blade. Section 6 concludes the paper.

2. SEC for surface strain monitoring

The SEC technology is described in details in [6]. Briefly, a soft nanocomposite constitutes its dielectric, onto which a conductive paint is applied to create the electrodes. Figure 1(*a*) shows the picture of an SEC (only one electrode is shown, in

black). Its schematic representation is provided in figure 1(*b*). The sensor has been designed to be adhered onto surfaces using off-the-shelf epoxies, along the *x*–*y* plane (figure 1(*b*)). Strains in the *x* or *y* direction provoke a change in the sensor's geometry, which can be measured via a change in the sensor's capacitance.

At low measurement frequency (<1 kHz), the SEC can be approximated as a non-lossy capacitor:

$$C = e_0 e_r \frac{A}{h_d}, \tag{1}$$

where C is the capacitance, $A = w \cdot l$ is the sensor area of width w and length l, h_d is the thickness of the dielectric, $e_0 = 8.854\,\mathrm{pF\,m^{-1}}$ is the vacuum permittivity, and e_r is the relative permittivity of the polymer. Assuming small strain, equation (1) can be differentiated:

$$\frac{\Delta C}{C} = \left(\frac{\Delta l}{l} + \frac{\Delta w}{w} - \frac{\Delta h}{h}\right) = \varepsilon_x + \varepsilon_y - \varepsilon_z, \tag{2}$$

where ε_x, ε_y and ε_z are the three principal directional strains as shown in figure 1(*b*). Assuming no external stress along the z direction, one can use Hooke's Law to obtain an expression for ε_z:

$$\varepsilon_z = -\frac{\nu}{1-\nu}(\varepsilon_x + \varepsilon_y), \tag{3}$$

where ν is the Poisson's ratio of the SEC. Substituting equation (3) into (2) gives the following electromechanical model:

$$\frac{\Delta C}{C} = \lambda(\varepsilon_x + \varepsilon_y), \tag{4}$$

where $\lambda = 1/(1-\nu)$ is the gauge factor ($\lambda \approx 2$ for the SEC). Equation (4) evidences that the sensor measures additive in-plane strains.

3. Algorithm for strain decomposition

The algorithm presented in this section is specialized for application to wind turbine blades. It is based on thin plate and shell structures theory, where shear deformation is assumed to be insignificant compared with bending deformations. Such assumption is common in the literature in modeling of wind turbine blades, and has been shown to provide accurate results [32]. Note that the algorithm can be extended to other types of structures by varying the strain-displacement relationships derived below (equations (8) and (9)), and by modifying the formulation defining deflection (equation (5)).

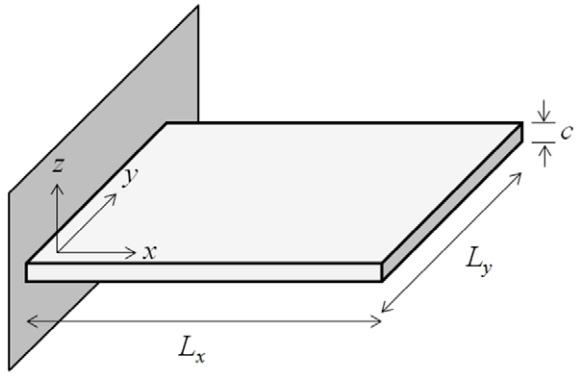

Figure 2. Schematic representation of a cantilever thin plate.

3.1. Algorithm formulation

Consider the cantilever plate shown in figure 2. The following nth order polynomial function can be used to approximate its deflection shape:

$$w(x, y) = \sum_{i=1,j=0}^{n} a_{ij} x^i y^j, \tag{5}$$

where w is the deflection, and a_{ij} are coefficients. Note that $i \neq 0$ is used to satisfy the displacement boundary condition on the clamped edge ($w(0, y) = 0$).

The displacement $w_k(x, y)$ at any sensor k can be represented in matrix notation:

$$\mathbf{W} = \mathbf{H}\mathbf{A}, \tag{6}$$

where $\mathbf{W} \in \mathcal{R}^{m\times 1}$ is the displacement vector, $\mathbf{H} \in \mathcal{R}^{m\times n(n+1)}$ is the location matrix, $\mathbf{A} \in \mathcal{R}^{n(n+1)\times 1}$ is the coefficient vector, and m is the number of sensors in the sensor network:

$$\begin{aligned}
\mathbf{W} &= [w_1 \ldots w_k \ldots w_m]^{\mathrm{T}}, \\
\mathbf{H} &= \begin{bmatrix} x_1 & x_1y_1 & \cdots & x_1y_1^n & x_1^2 & x_1^2y_1 & \cdots & x_1^2y_1^n & \cdots & x_1^n & x_1^ny_1 & \cdots & x_1^ny_1^n \\ \vdots & \vdots & \vdots & \vdots & \vdots & \vdots & \vdots & \vdots & \vdots & \vdots & \vdots & \vdots & \vdots \\ x_m & x_my_m & \cdots & x_my_m^n & x_m^2 & x_m^2y_m & \cdots & x_m^2y_m^n & \cdots & x_m^n & x_m^ny_m & \cdots & x_m^ny_m^n \end{bmatrix}, \\
\mathbf{A} &= [a_{10} \ldots a_{ij} \ldots a_{nn}]^{\mathrm{T}}.
\end{aligned} \tag{7}$$

Surface strain functions can be obtained from equation (5):

$$\varepsilon_x = -\frac{c}{2}\frac{\partial^2 \mathbf{W}}{\partial x^2} = \mathbf{H}_x \mathbf{A}_x, \tag{8}$$

$$\varepsilon_y = -\frac{c}{2}\frac{\partial^2 \mathbf{W}}{\partial y^2} = \mathbf{H}_y \mathbf{A}_y, \tag{9}$$

and written in terms of sensors' signals:

$$\mathbf{S} = [s_1 \ \ldots \ s_k \ \ldots \ s_m]^{\mathrm{T}} = \varepsilon_x + \varepsilon_y = \mathbf{H}_s \mathbf{A}_s, \tag{10}$$

where, for convenience, the signal s_k for the kth sensor is taken as:

$$s_k = \frac{\Delta C_k}{\lambda C_k} = \varepsilon_{x,k} + \varepsilon_{y,k} \tag{11}$$

and $\mathbf{S} \in \mathcal{R}^{m\times 1}$ is the sensor signal vector, $\mathbf{A} = [\mathbf{A}_0 | \mathbf{A}_s]$, $\mathbf{H} = [\mathbf{H}_0 | \mathbf{H}_s]$ with $\mathbf{A}_0$ and $\mathbf{H}_0$ representing terms in equation (6) that vanish upon double differentiation. Note that $\mathbf{A}_x$ and $\mathbf{A}_y$ are subsets of $\mathbf{A}_s$.

The parameter vector $\mathbf{A}_s$ is estimated using an LSE:

$$\hat{\mathbf{A}}_s = (\mathbf{H}_s^{\mathrm{T}} \mathbf{H}_s)^{-1} \mathbf{H}_s^{\mathrm{T}} \mathbf{S}, \tag{12}$$

where the hat denotes an estimation. In its unaltered form, $\mathbf{H}_s$ is multi-collinear because $\mathbf{H}_x$ and $\mathbf{H}_y$ share multiple columns. Matrix $\mathbf{H}_s^{\mathrm{T}}\mathbf{H}_s$ is therefore singular and non-invertible. To enable full rank of $\mathbf{H}_s^{\mathrm{T}}\mathbf{H}_s$, boundary conditions on the strain map need to be included within $\mathbf{H}_s$. This is done by altering the row of $\mathbf{H}_s$ associated with the kth sensor subjected to a particular boundary condition. These are discussed in what follows for the specialized case of a cantilever plate.

3.2. Boundary conditions for cantilever plate

The displacement boundary conditions are satisfied through the formulation of equation (5) via the selection of appropriate null coefficients. A similar strategy is used for enforcing the boundary conditions on rotation using the partial derivatives of equation (5). In particular, it is assumed here that the plate does not displace nor rotate at the root. The enforcement of the assumptions on the strain boundary conditions needs to be conducted on the second derivatives of the equation as discussed in section 3.1. For instance, for the cantilever plate shown in figure 2, we assume the following boundary conditions:

(1) $\varepsilon_y(0,\ \alpha_y \le y \le L_y - \alpha_y) = 0;$

(2) $\varepsilon_y(\alpha_x \le x \le L_x - \alpha_x,\ 0) = \varepsilon_y(\alpha_x \le x \le L_x - \alpha_x,\ L_y)$
$= -\nu_m \varepsilon_x$ by taking $\sigma_y = 0$;

(3) $\varepsilon_x(L_x,\ \alpha_y \le y \le L_y - \alpha_y) = -\nu_m \varepsilon_y$ by taking $\sigma_x = 0$;

where ν_m is the Poisson's ratio of the plate, α_x and α_y are constants such that $0 \le \alpha_x \le L_x$ and $0 \le \alpha_y \le L_y$ to account for different boundary conditions at corners [33, 34].

After enforcing these constraints, $\hat{\mathbf{A}}_s$ can be obtained from equation (12), which includes the estimated parameters $\hat{\mathbf{A}}_x$ and $\hat{\mathbf{A}}_y$. This allows the decomposition of the strain components using equations (8) and (9). The deflection shape can also be estimated through equation (6) after solving $\mathbf{A}_0$ using the boundary conditions on displacement and rotation at the clamped edge.

3.3. Experimental validation

The proposed algorithm is validated on a small scale laboratory experiment. The inexpensive off-the-shelf capacitance data acquisition system (ACAM PCap02) used for the experiment only measures up to eight capacitors (including a reference), which limits the number of SECs used in the experimental procedure. In this experiment, six SECs are deployed on a cantilever fiber glass plate of dimensions ($457 \times 324 \times 3.2\,\mathrm{mm}^3$). Resistive strain gauges (RGS) (TML Strain Gauges type FLA-6-11-3LT) are installed along each edge of each SEC to verify measurements. Data from the RGS are acquired using a Hewlett-Packard 2850 data acquisition system and sampled at 1.7 Hz, while data from the SECs are sampled at 20 Hz. Two load configurations are considered: (1) a point load at the center tip; and (2) a point load at a corner. These two load configurations are consistent with loads used in the numerical simulations (section 4). They were applied sequentially while taking continuous measurements. Figure 3 shows the laboratory test configuration. Data from the SECs are compared against the average value of RSG measurements located on all four sides of each sensor.

Figure 4 shows the strain values acquired from each SEC using equation (4). They are compared against the theoretical reading from the summing readings from surrounding RSGs. The time series counts five plateaus. The first three plateaus are used to calibrate the sensor (accurately establishing C_0). The fourth plateau show results from the application of the center load, while the fifth plateau show results from the application of the corner load. Time series results show a good fit between the SECs and the RSGs approximately within the reported resolution of $25\mu\varepsilon$ in [6], validating the electromechanical model.

Given the low number of sensors used in this laboratory verification, the boundary conditions can only be enforced on one or two sensors in order to demonstrate the algorithm. In addition, because the monitored plate itself is small compared with possible full-scale applications, the sensors are relatively far from the edge which adds error in the boundary condition assumptions. For both load cases, the only assumed boundary condition is $\varepsilon_y = 0$ at the fixed edge (thus for sensors C and F). The average values at each plateau for each SEC are taken as input for the algorithm. The decomposition is conducted using a deflection shape (equation (5)) of the fourth order in x and third order in y given the low number of sensors used on the plate.

Tables 1 and 2 show the decomposition results compared with the average results acquired form the RSGs located on both sides of each sensors in each directions, for the center and corner load cases, respectively. Results show an overall acceptable performance for both load cases for computing principal strain component values, except for sensor D that showed a substantial overestimation. Factors that contribute to larger discrepancies include (1) the signal-to-noise ratio in the SEC signal, which is notably observable in figure 4 for

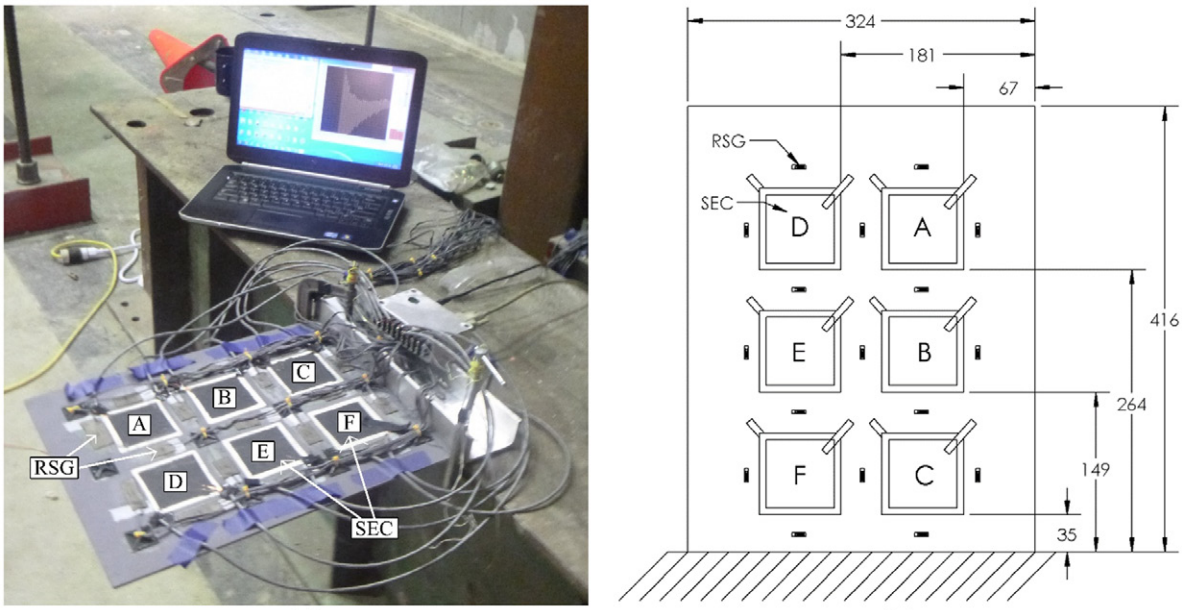

(a) (b)

Figure 3. Laboratory test configuration: (*a*) picture; and (*b*) schematic. Distances are in mm.

Table 1. Center load (units are in $\mu\varepsilon$).

Sensor	ε_x	$\widehat{\varepsilon}_x$	$\lvert\varepsilon_x - \widehat{\varepsilon}_x\rvert$	ε_y	$\widehat{\varepsilon}_x$	$\lvert\varepsilon_y - \widehat{\varepsilon}_y\rvert$
A	186.9	177.8	9.02	– 54.78	– 77.82	23.04
B	366.8	330.0	36.8	– 33.10	5.93	39.03
C	574.4	559.9	14.4	– 24.85	0.00	24.85
D	202.1	411.3	209.1	– 49.51	– 252.5	203.0
E	383.8	423.1	39.21	– 24.72	– 82.18	57.46
F	572.3	512.6	59.77	– 20.27	0.00	20.27

Table 2. Corner load (units are in $\mu\varepsilon$).

Sensor	ε_x	$\widehat{\varepsilon}_x$	$\lvert\varepsilon_x - \widehat{\varepsilon}_x\rvert$	ε_y	$\widehat{\varepsilon}_x$	$\lvert\varepsilon_y - \widehat{\varepsilon}_y\rvert$
A	136.0	185.5	49.50	38.18	– 11.62	49.80
B	341.7	339.8	1.90	9.74	10.89	1.14
C	534.1	542.8	8.69	0.65	0.00	0.65
D	165.5	385.4	219.9	37.12	– 178.1	215.2
E	374.0	465.0	91.01	19.15	– 77.22	96.37
F	589.8	593.3	3.48	– 5.56	0.00	5.56

sensor D; (2) the weak assumption on the boundary condition for sensors C and F, in particular for the center load case; and (3) the load number of sensors used in the experiment, which limits the application of a consistent polynomial (equation (5)) and additional boundary conditions. Nevertheless, this laboratory experiment demonstrates the promise of the algorithm at decomposing principal strain components.

4. Simulations: symmetric plate

This section verifies the performance of the strain decomposition algorithm on an isotropic rectangular cantilever thin plate under different static loads. The influence of the order of the polynomial defining the deformation (equation (5)) and the robustness of the algorithm under different noise levels are examined as well as computing time.

4.1. Numerical model

The simulated model consists of a cantilever aluminum thin plate, with SECs deployed in a network configuration. Two load cases are studied: load case 1 is a point load of 2 kN at the center tip to produce a symmetric response; and load case 2 is a 1.5 kN load at a corner to produce torsion. Each SEC is assumed to have a size of $70 \times 70\,\mathrm{mm}^2$, similar to a typical size (figure 1(*a*)). Figure 5 shows the numerical model. Each square in figure 5 denotes an SEC, the filled circles denote the centroid of a sensor, red circles denote a sensor subjected to boundary conditions (discussed in section 3.2), and blue

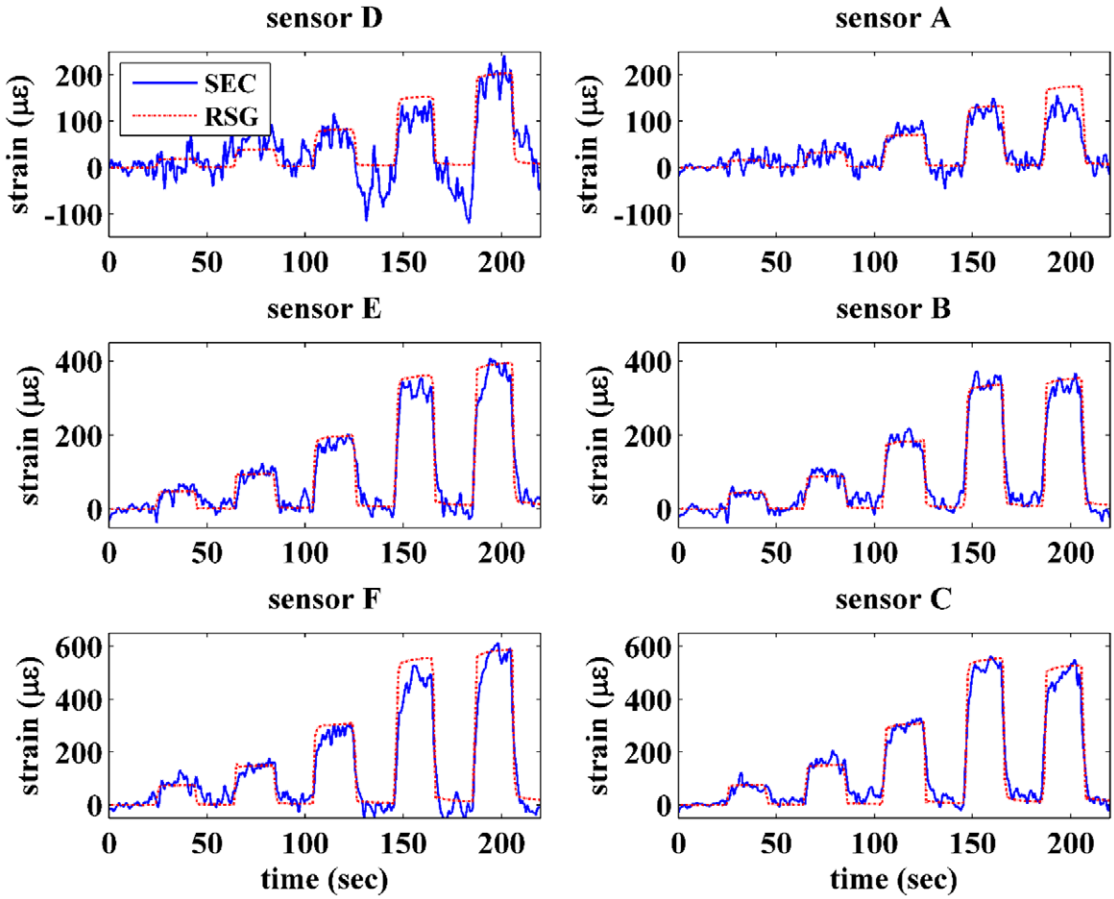

Figure 4. Strain values obtained from SECs plotted against RSG results.

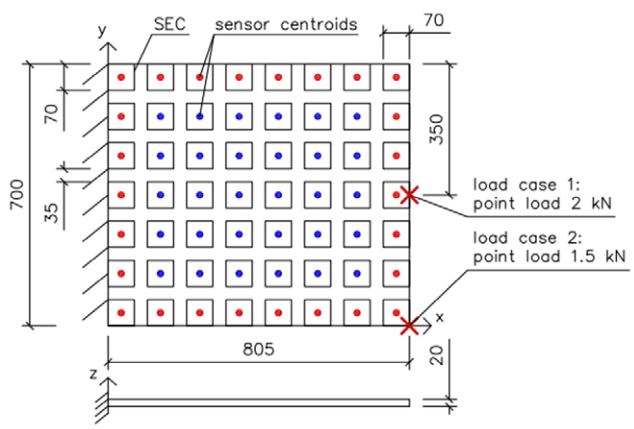

Figure 5. Simulated symmetric plate model. Distances are in mm.

circles denote sensors not subjected to boundary conditions. A 2% Gaussian noise is introduced in the simulated SEC signals (constructed with equation (11)); the surface strains in two principal directions are reconstructed using equations (8) and (9); and the deflection shapes are reconstructed using equation (6). The algorithm is verified with the highest polynomial order possible with the selected sensor arrangement ($n = 6$). The absolute percentage error (APE) and mean APE (MAPE) are used as performance measures for the algorithm. The APE is used to compare fitting results over a contour map, while the MAPE is used to compare the overall fitting results over the entire plate.

4.2. Strain decomposition

Figure 6 compares the APE of the strain decomposition results for strains ε_x and ε_y in the two principal directions of the cantilever plate under load cases 1 and 2. Results are shown for the SECs not subjected to boundary conditions (blue circles in figure 5). The algorithm performs well at estimating surface strain along the x-axis, which dominates the bending behavior. This fitting performance is lower at the free corners and at the load location. This can be caused by corner singularities and local shear stress caused by point load which introduce more error in the assumptions on the strain boundary conditions and plane stress assumption for thin plate. Also, the boundary conditions are applied at the modeled boundary sensor nodes which are not located directly on the boundaries. Figures 6(*b*) and (*d*) show a higher APE for the estimation of the surface strain along y-axis under both load cases. This can be caused by a higher dependence of ε_y on the boundary condition assumptions, which are less accurate at the free-end corners. In addition, the APE of ε_y is more significant under torsion (load case 2) at localized region on the clamped edge.

The three-dimensional (3D) maps of strain decomposition results for load case 1 and 2 are shown in figure 7. While the APE suggests regions of larger errors, the 3D strain maps

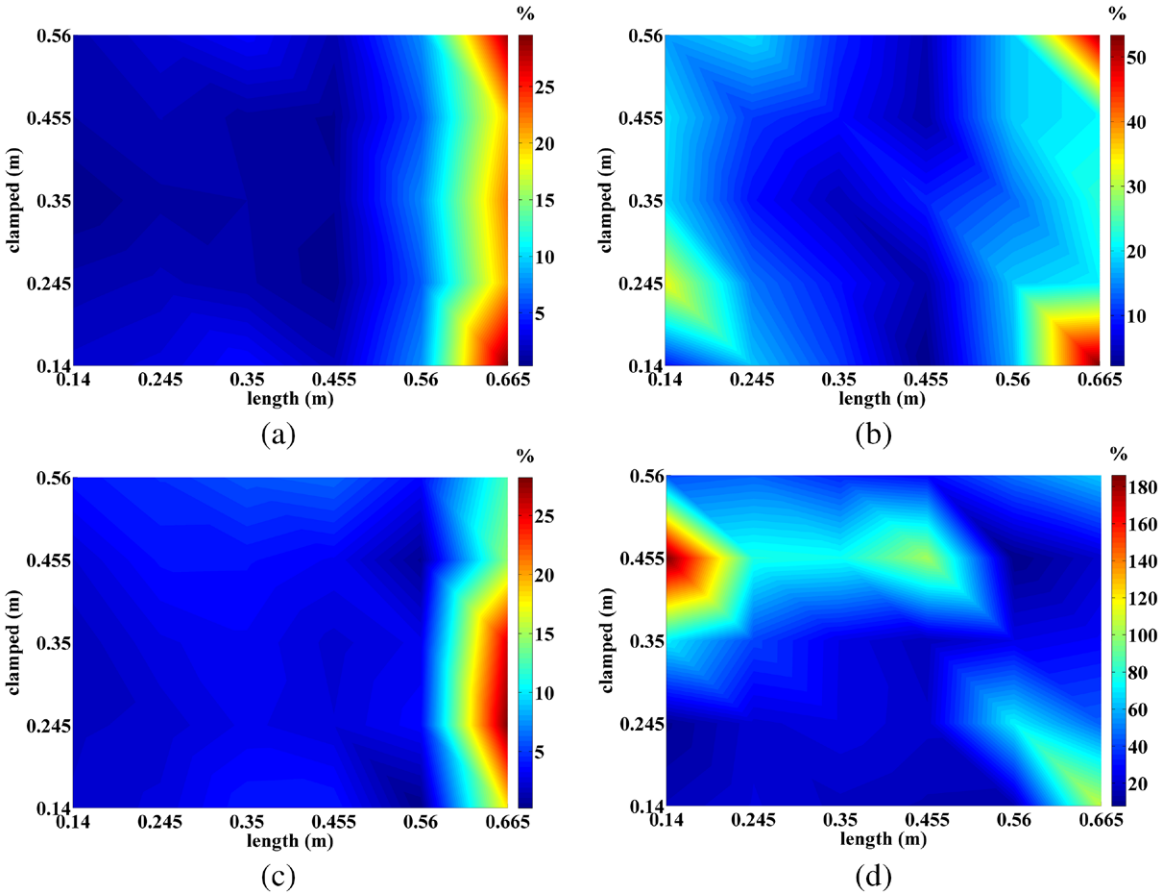

Figure 6. APE contour within plate boundary: (*a*) APE-ε_x under load case 1; (*b*) APE-ε_y under load case 1; (*c*) APE-ε_x under load case 2; (*d*) APE-ε_y under load case 2.

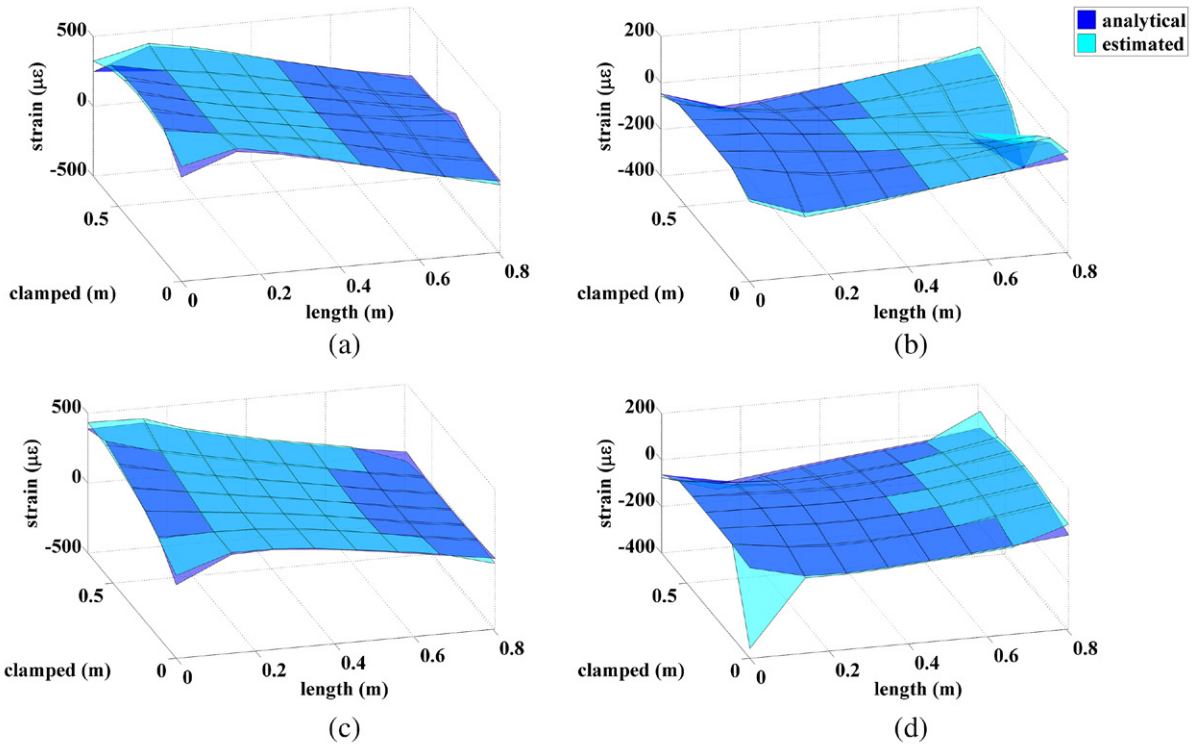

Figure 7. 3D strain map over full plate surface: (*a*) ε_x under load case 1; (*b*) ε_y under load case 1; (*c*) ε_x under load case 2; (*d*) ε_y under load case 2.

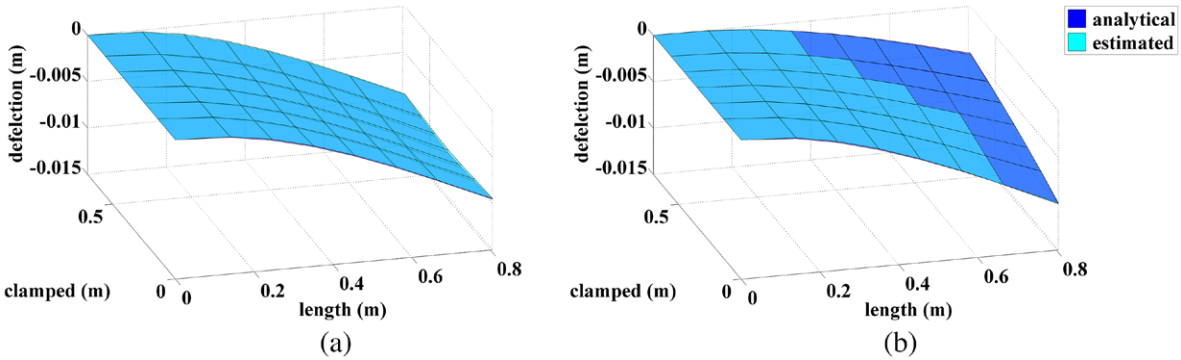

Figure 8. (*a*) Deflection shape under load case 1; (*b*) Deflection shape under load case 2.

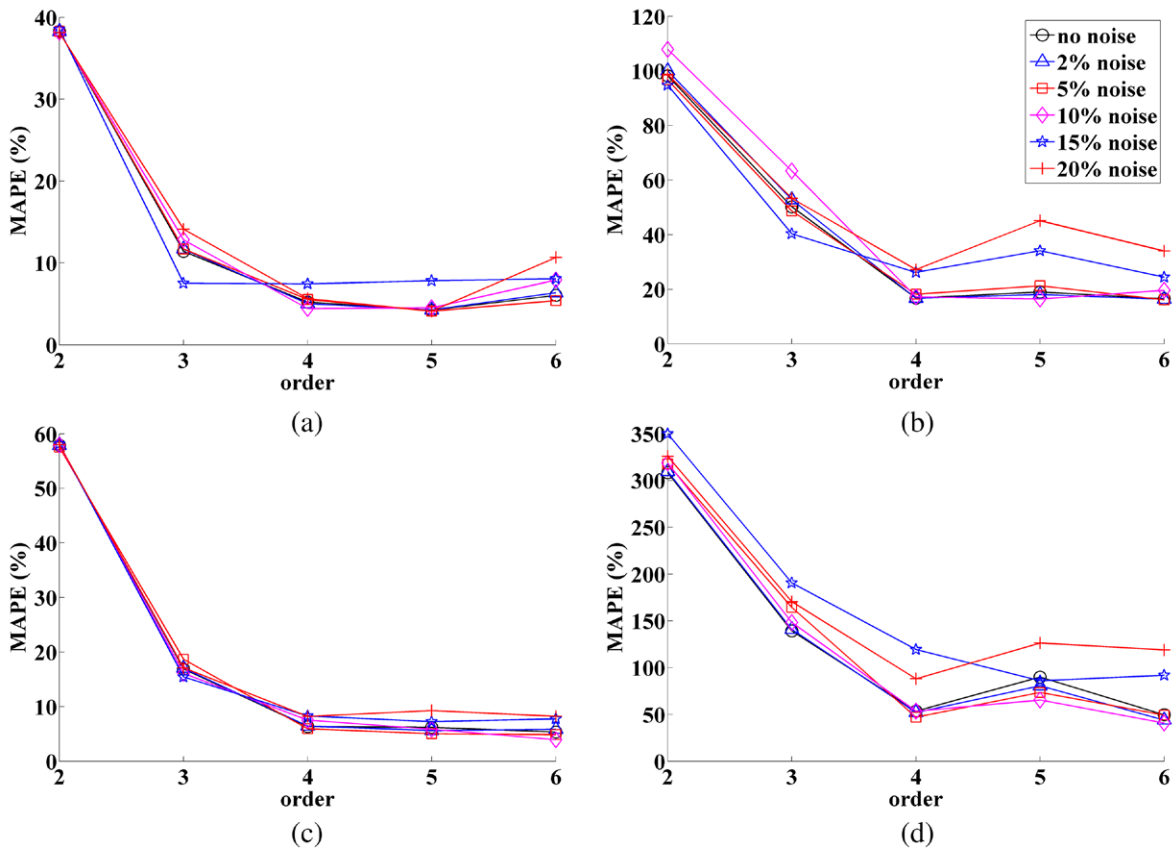

Figure 9. Variation of MAPE versus polynomial order and noise level: (*a*) MAPE-ε_x under load case 1; (*b*) MAPE-ε_y under load case 1; (*c*) MAPE-ε_x under load case 2; (*d*) MAPE-ε_y under load case 2.

display a good agreement in the overall shape, with the largest errors located at the plate boundaries. This shows the high dependence of the algorithm on the assumptions made on the boundary conditions. Figure 8 shows the deflections shapes reconstructed using equation (6) for both load cases. There is good agreement between the analytical and estimated results. The MAPE of deflection shapes is 4.76% for load case 1 and 2.62% for load case 2. The error around the point load location can also be of particular interest given the possible error introduced by the inapplicability of the thin plate in-plane stress assumption. The APE is 3.10% for load case 1 and 3.31% for load case 2 directly at the point load location, and the MAPE at the neighbor sensor nodes is 2.60% and 1.57% for load cases 1 and 2, respectively. The assumption of thin plate deformation provided a good estimation for the reconstruction of strain maps.

Table 3. Computing time as a function of the polynomial order.

Order level	2nd	3rd	4th	5th	6th
Computing time (ms)	7.89	8.41	8.58	8.74	9.02

4.3. Polynomial order and noise

This performance of the algorithm with respect to the polynomial order of the deflection shape (equation (5)) and signal noise is examined. Figure 9 shows the MAPE of the estimation results for all the non-boundary sensors versus the polynomial order

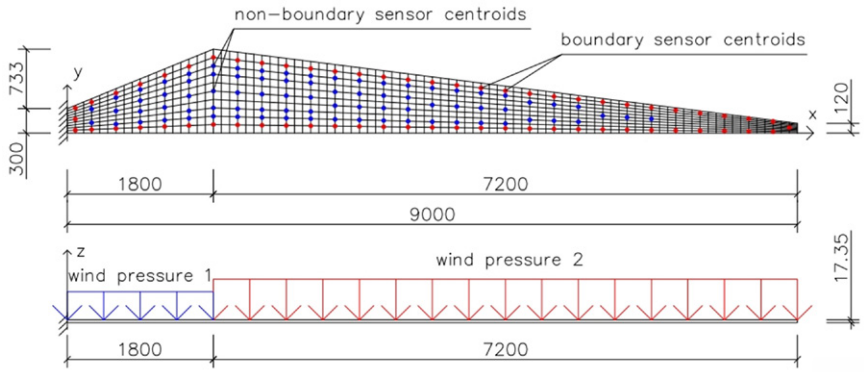

Figure 10. Simulated asymmetric plate model. Dimensions are in mm.

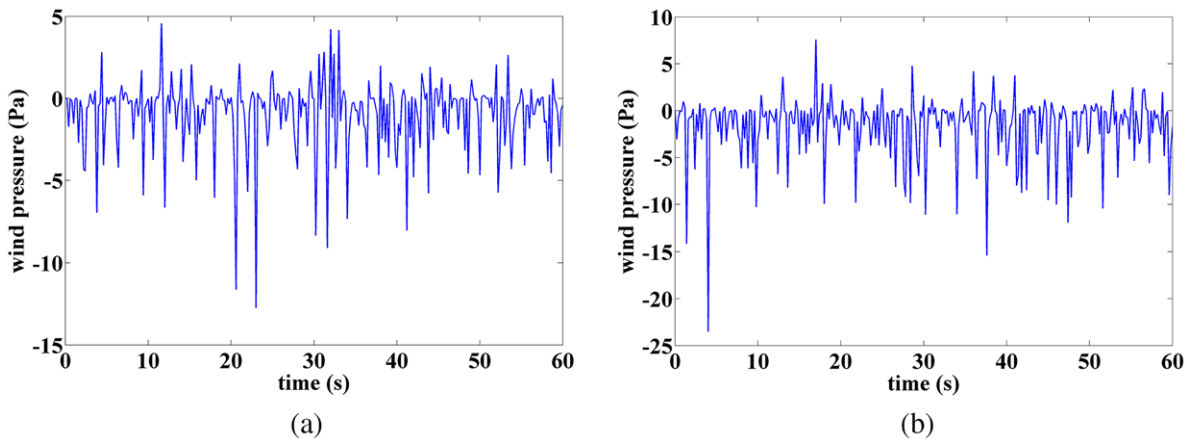

Figure 11. Time histories of simulated wind loads: (*a*) wind pressure 1; (*b*) wind pressure 2.

and noise level for load case 1 and 2. The order of the polynomial varies from a second order to a sixth order, the highest possible order given the number and configuration of the SEC network (figure 5). The investigated noise levels are 0, 2, 5, 10, 15 and 20% Gaussian noise. Results show that at least a fourth order polynomial is required to provide an adequate performance. Increasing the polynomial order beyond this point provides a marginal increase in performance for most cases. Also, the algorithm appears to be stable under noise levels below 10%.

The influence of the polynomial order on the computation time is shown in table 3. Simulations were conducted in MATLAB using a 2.50 GHz Intel CPU. Increasing the order of the polynomial does not significantly increase computing time. The longest computing time of 9.02 ms enables a real-time application for a typical sampling frequency below 100 Hz. Note that this performance can be improved by using different software, code, and computing platform.

5. Simulations: asymmetric plate

5.1. Numerical model

Numerical simulations are extended to an asymmetric plate mimicking a wind turbine blade. The 9 m cantilever thin plate is constituted with laminated sections of orthotropic materials as defined in [35]. The model is subjected to two time varying wind pressures on two separated areas. The simulated asymmetric plate model along with the configuration of the SEC network is shown in figure 10. Similarly to figure 5, the red circles denote the sensors subjected to boundary conditions, and the blue circles denote the sensors not subjected to boundary conditions. Two sets of non-stationary wind pressure time series were produced at 5 Hz over 60 s using a dual approach based on low frequency measured real wind speed data and turbulence spectrum [36, 37]. Time histories are shown in figure 11.

5.2. Strain decomposition

Figure 12 shows the time series of the MAPE for the sensors not subjected to boundary conditions (blue circles in figure 10). During most of the wind excitation, the MAPE of both ε_x and ε_y remains approximately constant and low: around 3% for ε_x and 12% for ε_y. The fit on strain ε_y has a much higher variability in results, as it would be expected from the simulation results discussed in the previous section. Nevertheless, the generally constant error and its relatively low level demonstrate stability of the algorithm with respect to a time-varying excitation. The higher value peaks in the MAPE coincide with sensor signals close to zero for the majority of sensors, which cause over-fitting from the LSE algorithm. A possible alternative would be to apply a different fitting algorithm when

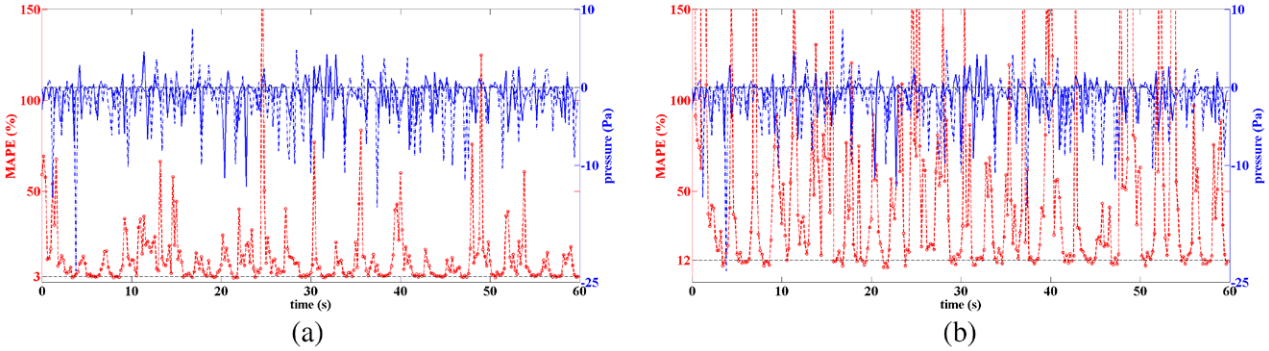

Figure 12. MAPE of time histories: (*a*) ε_x; (*b*) ε_y.

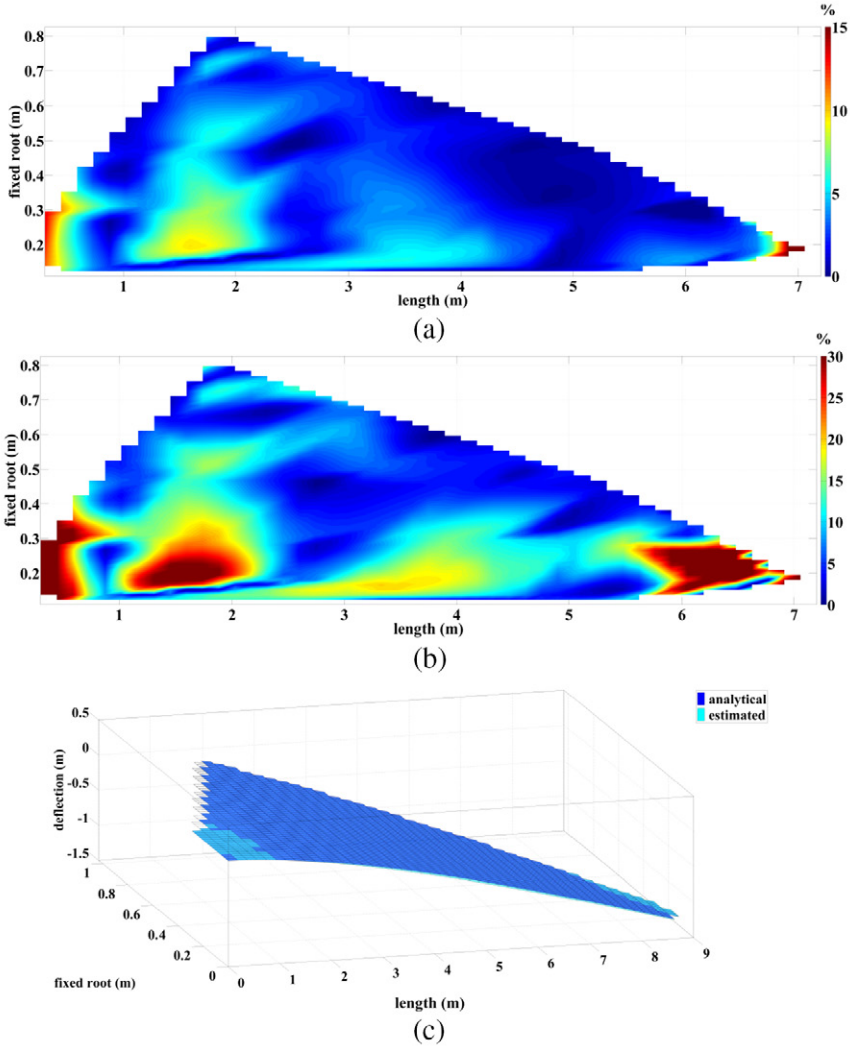

Figure 13. Strain decomposition results at 30 s: (*a*) APE-ε_x; (*b*) APE-ε_y; (*c*) deflection shape.

several sensors output measurements close to zero. This is out of the scope of this paper.

Figure 13 shows the APE contours for a typical simulation result when the MAPE is stable (taken at 30 s). Unlike for the symmetric plate case, both the APE contours of the estimation of ε_x and ε_y suggest a relatively higher error at the fixed root. This can be attributed to the error in the assumptions on the boundary conditions caused by an irregular geometry. The APE on most regions of the plate remains under 5% for ε_x and under 15% for ε_y. Figure 13(*c*) is a 3D plot of the deflection shape, showing good agreement between the estimated and analytical results. The MAPE for the deflection shape is 2.70% and the maximum APE is 12.14% over the entire surface.

6. Conclusions

We have presented a novel sensor for surface strain measurements. Used in a network configuration, SECs can be used to cover mesosurfaces, and measurements used to reconstruct physics-based features for condition assessment, such as strain maps and deflection shapes. Given that each SEC measures additive strain from both principal directions, an algorithm was developed to retrieve the magnitude and directional information of strain prior to reconstructing strain maps. The algorithm assumes a polynomial displacement shape, and an LSE is used to estimate the coefficients of the polynomial after enforcement of the boundary conditions. Given the proposed engineering application to wind turbine blades, the algorithm was specialized for thin plates and shell structures. The performance of the algorithm has been verified on a symmetric cantilever thin plate with SECs arranged in a network configuration. Further investigations have been conducted on an asymmetric cantilever laminated thin plate with orthotropic materials mimicking a wind turbine blade, subjected to a non-stationary wind load. Results showed a good robustness and accuracy of the algorithm under most loading conditions, except when most of the sensors' signals are close to zero.

While results demonstrate the overall promise of the algorithm, refining the assumptions on the boundary conditions and developing strategies to cope with corner singularities have the potential to substantially improve its accuracy. Future work could include a dual form that would eliminate over-fitting from the LSE when the sensors' signals are close to zero.

We have showed that the sensor network can be used to produce 2D strain maps and deflection shapes, in real-time and for noise levels under 10%. The study of temporal and spatial changes in these maps and shapes could be used for real-time condition assessment of mesosystems. This would significantly empower system managers and owners by enabling timely maintenance and optimizing of operations.

Acknowledgments

This work is supported from the Iowa Alliance for Wind Innovation and Novel Development (IAWIND) (Grant 1001062565), and the Iowa Energy Center (Grant 13-02). Their support is gratefully acknowledged.

References

[1] Farrar C R and Lieven N A 2007 Damage prognosis: the future of structural health monitoring *Phil. Trans. R. Soc.* A **365** 623–32

[2] Laflamme S, Kollosche M, Connor J J and Kofod G 2012 Robust flexible capacitive surface sensor for structural health monitoring applications *J. Eng. Mech.* **139** 879–85

[3] Adams D, White J, Rumsey M and Farrar C 2011 Structural health monitoring of wind turbines: method and application to a HAWT *Wind Energy* **14** 603–23

[4] Chang P C, Flatau A and Liu S 2003 Review paper: health monitoring of civil infrastructure *Struct. Health Monitoring* **2** 257–67

[5] Ciang C C, Lee J-R and Bang H-J 2008 Structural health monitoring for a wind turbine system: a review of damage detection methods *Meas. Sci. Technol.* **19** 122001

[6] Laflamme S *et al* 2013 Soft elastomeric capacitor network for strain sensing over large surfaces *Mechatronics, IEEE/ASME Transactions* **18** 1647–54

[7] Laflamme S, Kollosche M, Kollipara V D, Saleem H S and Kofod G 2012 Large-scale surface strain gauge for health monitoring of civil structures *SPIE Smart Structures and Materials + Nondestructive Evaluation and Health Monitoring* International Society for Optics and Photonics p 83471P

[8] Hu Y *et al* 2014 Large-scale sensing system combining large-area electronics and CMOS ICs for structural-health monitoring *IEEE J. Solid-State Circuits* **49** 513–23

[9] Tung S, Yao Y and Glisic B 2014 Sensing sheet: the sensitivity of thin-film full-bridge strain sensors for crack detection and characterization *Meas. Sci. Technol.* **25** 075602

[10] Gao L, Thostenson E T, Zhang Z, Byun J-H and Chou T-W 2010 Damage monitoring in fiber-reinforced composites under fatigue loading using carbon nanotube networks *Phil. Mag.* **90** 4085–99

[11] Kang I, Schulz M J, Kim J H, Shanov V and Shi D 2006 A carbon nanotube strain sensor for structural health monitoring *Smart Mater. Struct.* **15** 737

[12] Loh K J, Kim J, Lynch J P, Kam N W S and Kotov N A 2007 Multifunctional layer-by-layer carbon nanotube–polyelectrolyte thin films for strain and corrosion sensing *Smart Mater. Struct.* **16** 429

[13] Srivastava R K *et al* 2011 The strain sensing and thermal–mechanical behavior of flexible multi-walled carbon nanotube/polystyrene composite films *Carbon* **49** 3928–36

[14] Suster M, Guo J, Chaimanonart N, Ko W H and Young D J 2006 A high-performance MEMS capacitive strain sensing system *J. Microelectromech. Syst.* **15** 1069–77

[15] Lipomi D J *et al* 2011 Skin-like pressure and strain sensors based on transparent elastic films of carbon nanotubes *Nat. Nanotechnol.* **6** 788–92

[16] Dobrzynska J A and Gijs M 2013 Polymer-based flexible capacitive sensor for three-axial force measurements *J. Micromech. Microeng.* **23** 015009

[17] Harrey P, Ramsey B, Evans P and Harrison D 2002 Capacitive-type humidity sensors fabricated using the offset lithographic printing process *Sensors Actuators* B **87** 226–232

[18] Hong H P, Jung K H, Min N K, Rhee Y H and Park C W 2012 A highly fast capacitive-type humidity sensor using percolating carbon nanotube films as a porous electrode material *Proc. IEEE Sensors (Taipei, Taiwan, October 2012)* pp 1–4

[19] Goldrein H, Palmer S and Huntley J 1995 Automated fine grid technique for measurement of large-strain deformation maps *Opt. Lasers Eng.* **23** 305–18

[20] Pan B, Qian K, Xie H and Asundi A 2009 2D digital image correlation for in-plane displacement and strain measurement: a review *Meas. Sci. Technol.* **20** 062001

[21] Tessler A and Spangler J L 2003 *A Variational Principle for Reconstruction of Elastic Deformations in Shear Deformable Plates and Shells* (NASA, Langley Research Center: Edwards, CA, United States)

[22] Tessler A and Spangler J L 2004 Inverse FEM for full-field reconstruction of elastic deformations in shear deformable plates and shells *Proc. 2nd European Workshop on Structural Health Monitoring* pp 83–90

[23] Tessler A and Spangler J L 2005 A least-squares variational method for full-field reconstruction of elastic deformations in shear-deformable plates and shells *Comput. Methods Appl. Mech. Eng.* **194** 327–39
[24] Derkevorkian A, Masri S F, Alvarenga J, Boussalis H, Bakalyar J and Richards W L 2013 Strain-based deformation shape-estimation algorithm for control and monitoring applications *AIAA J.* **51** 2231–40
[25] Ko W L and Fleischer V T 2013 Method for estimating operational loads on aerospace structures using span-wisely distributed surface strains
[26] Ko W L, Richards W and Tran V T 2007 *Displacement theories for in-flight deformed shape predictions of aerospace structures* (NASA Dryden Flight Research Center: Edwards, CA, United States) 214612
[27] Rajalingham C, Bhat R and Xistris G 1996 Vibration of rectangular plates using plate characteristic functions as shape functions in the Rayleigh–Ritz method *J. Sound Vibration* **193** 497–509
[28] Tian B, Zhong Y and Li R 2011 Analytic bending solutions of rectangular cantilever thin plates *Archives Civil Mech. Eng.* **11** 1043–52
[29] Zhong Y, Zhao X-F and Li R 2013 Free vibration analysis of rectangular cantilever plates by finite integral transform method *Int. J. Comput. Methods Eng. Sci. Mech.* **14** 221–6
[30] Jones R *et al* 1998 Determination of cantilever plate shapes using wavelength division multiplexed fiber Bragg grating sensors and a least-squares strain-fitting algorithm *Smart Mater. Struct.* **7** 178
[31] Lancaster P and Salkauskas K 1986 *Curve and Surface Fitting* (New York: Academic)
[32] Bazilevs Y, Hsu M C, Kiendl J, Wüchner R and Bletzinger K U 2011 3D simulation of wind turbine rotors at full scale: II. Fluid–structure interaction modeling with composite blades *Int. J. Numer. Methods Fluids* **65** 236–53
[33] Huang C 2003 Stress singularities at angular corners in first-order shear deformation plate theory *Int. J. Mech. Sci.* **45** 1–20
[34] McGee O, Leissa A and Huang C 1992 Vibrations of cantilevered skewed trapezoidal and triangular plates with corner stress singularities *Int. J. Mech. Sci.* **34** 63–84
[35] Berry D and Ashwill T 2007 Design of 9-meter carbon-fiberglass prototype blades: CX-100 and TX-100 *SAND* 2007-0201 Sandia National Laboratories, Albuquerque, NM
[36] Rose S and Apt J 2012 Generating wind time series as a hybrid of measured and simulated data *Wind Energy* **15** 699–715
[37] Service N W *Physical Oceanographic Real-Time System* 9414290 San Francisco, CA